On performance of thin-film meso-structured perovskite solar cell through experimental analysis and device simulation

F. Bonnín-Ripoll [a, *], Y.B. Martynov [b], R.G. Nazmitdinov [c, d], K. Tabah [e], C. Pereyra [e], M. Lira-Cantú [e], G. Cardona [f], R. Pujol-Nadal [a]

[a] Departament d'Enginyeria Industrial i Construcció, Universitat de les Illes Balears, E-07122, Palma, Spain
[b] State Scientific-Production Enterprise "Istok", Fryazino, Russia
[c] Bogoliubov Laboratory of Theoretical Physics, Joint Institute for Nuclear Research, 141980, Dubna, Russia
[d] Dubna State University, 141982, Dubna, Moscow region, Russia
[e] Catalan Institute of Nanoscience and Nanotechnology (ICN2), CSIC and the Barcelona Institute of Science and Technology (BIST), Building ICN2, Campus UAB, E-08193, Bellaterra, Barcelona, Spain
[f] Departament de Matemàtiques, Universitat de les Illes Balears, E-07122, Palma, Spain

ARTICLE INFO

ABSTRACT

In the last few years, there has been an unprecedented progress in the increase of the power conversion efficiency of perovskite solar cells. Evidently, further advances in the efficiency of these devices will depend on the constraints imposed by the optical and electronic properties of their constituents. Quite apparently during the manufacturing process of a solar cell, there is an inevitable variation in the thicknesses of various functional layers, which affects the optoelectronic characteristics of the final sample. In this work, a possible strategy of the analysis of the solar cell performance is suggested, based on statistically averaging procedure of experimental data. We present a case study, in which the opto-electronic properties of the meso-structured perovskite solar cell (with a mesoporous TiO_2 layer) are analyzed within the method providing a deeper understanding of the device operation. This method enables an assessment of the overall quality of the device, pointing pathways towards the maximum efficiency design of a perovskite solar cell by material properties tuning.

1. Introduction

Nowadays organic-inorganic halide perovskites, as solar cell light-absorbers, attract substantial attention. Solar cells with such photoactive layers are considered as one of the most promising competitors to silicon-based photovoltaics, reaching efficiencies of 25.8% only in two decades of development [1]. Low-cost production of these materials with high power conversion efficiency (PCE) pledges fast development of flexible solar cells [2]. Moreover, there is a challenging future in improvement of their performance in order to reach their maximum efficiency (cf. [3]) by means of engineering of perovskite composition [4] or/and perovskite solar cell (PSC) constituents [5–9]; study and improvement of perovskite stability [10]; altering characteristics of optoelectronic behavior of PSC constituents [11] by incorporation, for example, light trapping mechanisms [12]; to name just a few.

Evidently, for further efficiency improvements of PSCs, the analysis of optical and electric properties of different layers in the device architecture is pivotal for optimizing light-harvesting in the absorber, whilst allowing coherent effects and parasitic absorption to be accounted in the stack design. In addition, this analysis should be based on statistically reliable estimates of noticeable dispersion of various sample parameters during the manufacturing process. Partially, some attempts in this direction have been made in Refs. [13–15], where various types of simulations of optoelectronic properties of PSCs have been conducted recently. It is worth noting that for the analysis of optical properties various research groups (see, for example, [16–20]) use the software SCAPS-1D [21] as a main tool. This code does not, however, consider interference, scattering, or intermediate reflectors (see details in Ref. [21]), thus preventing the comprehensive analysis of the antireflection layer's interference and the influence of thin film thicknesses.

* Corresponding author.
  E-mail address: f.bonnin@uib.cat (F. Bonnín-Ripoll).

Also, a broad range of electron (hole) transport materials and back metal contacts have been considered to examine the performance of lead-free PSCs in Ref. [22]. It also became common to introduce a mesoporous TiO$_2$ layer between TiO$_2$ electron collecting contact and perovskite (the main absorber layer). This process decreases defect density at the absorber boundary, while may introduce additional resistance. Nevertheless, the effect of a mesoporous TiO$_2$ layer and its influence on the PSC performance remains in infancy.

Here, we employ a ray tracing-based optoelectronic computational model [23] to reproduce the behavior of a PSC with a mesoporous TiO$_2$ layer and characterize experimental PSC samples. To this aim we further developed this model, incorporating a few novel elements to treat properly thin-film meso-structured PSCs.

The experimental device configuration (see Fig. 1) is selected as well-established, experimentally PSC [24]. The measurements of optical transmittance have been performed in each stage of the manufacturing process.

In this n-i-p junction device structure, apart from the complex glass substrate, a thin and compact TiO$_2$ (c-TiO$_2$) is manufactured as an electron selective contact to facilitate the collection of photogenerated electrons from perovskite absorber. Next, to improve the efficiency of carrier collection a mesoporous TiO$_2$ (mp-TiO$_2$) is introduced to provide a suitable perovskite deposition [25]. In addition, the partial infiltration of halide perovskite into the mp-TiO$_2$ layer facilitates higher quantum yield for photo-excited charge separation. Spiro-OMeTAD has been utilized in establishing a good p-contact between the gold (Au) counter electrode with a perovskite absorber in our stack design. As mentioned above, we will elaborate about the model [23] and discuss in detail the effective medium approach for analysis of the optical behavior of mp-TiO$_2$. Our approach is experimentally verified with measurements of the device reflection and transmission spectra. These characteristics have been measured by means of spectrophotometry techniques applied at each manufacturing stage. Finally, we make use of our approach to evaluate the dependence of the PSC performance on the properties of the mesoporous structure of the considered solar cell architecture, based on statistically averaged physical and geometrical parameters of the device.

2. Methodology

2.1. Device characteristics

Since electronic and optical measurements cannot be performed on the same PSC sample, we use two batches of 24 solar cells, manufactured at the same conditions. One batch is used for optical measurements with interruptions on each phase of the process, while the second one is used for J-V characteristic measurements without any interruptions on each phase of the process.

Considering the deposition of a material as a new phase of the process, we have performed the measurements of optical transmittance of each PSC layer in each stage of the manufacturing process (see details in Supplementary Material). Stage 1 of the manufacturing process consists of the glass substrate, assuming the material as a multilayer system itself, formed by sodalime glass, SnO$_2$, SiO$_2$, and fluorine-doped tin oxide (FTO). In stage 2, a layer of c-TiO$_2$ of the order of tens of nanometers is added by the spray pyrolysis technique. Next, a mp-TiO$_2$ layer is deposited in stage 3, followed by the subsequent deposition of a perovskite (stage 4) and Spiro-OMeTAD (stage 5), the latter three using the spin coating technique.

Next, using a solar simulator, the J-V characteristics of the PSCs in operation of a second batch of 24 solar cells has been measured. The result of this measurements provides the average value of the short-circuit current $J_{sc} = 20.07$ mA/cm^2 with a standard deviation 0.99 mA/cm^2 at irradiance 1000 W/m^2. In this study, we will focus on reproducing the behavior of the reverse scan of the J-V characteristics. The scanning process conditions are discussed in Ref. [24].

2.2. Optoelectronic model

To analyze the amount of transmitted, absorbed, and reflected light in each of the materials present in the PSCs, we employ ray tracing simulations with the aid of the ray trace OTSun python package [26,27]. It is a Monte Carlo ray tracing where the optics is implemented through the Fresnel optics equations in their most general form, complemented by the transfer-matrix method (TMM) to account for the interference phenomenon [28,29]. This software allows us to perform the simulations by loading a geometry file designed with the aid of FreeCAD [30], an open-source software for the parametric modeling of geometric figures in 3D.

The simulations require knowledge of the layer thicknesses as well as the complex refractive indexes of the corresponding materials as a function of wavelength (λ). In particular, the complex refractive indexes of the following materials have been taken from literature: FTO [31], TiO$_2$ [32], and Spiro-OMeTAD [33]. In the case of SnO$_2$ and SiO$_2$, the data are taken from the material manufacturer itself. According to the experimental setup [24] the chemical structure of the perovskite layer has been associated with FaPbI$_3$. In this case, the complex refractive index data are taken from Ref. [34], where the real and imaginary parts of the refractive index have
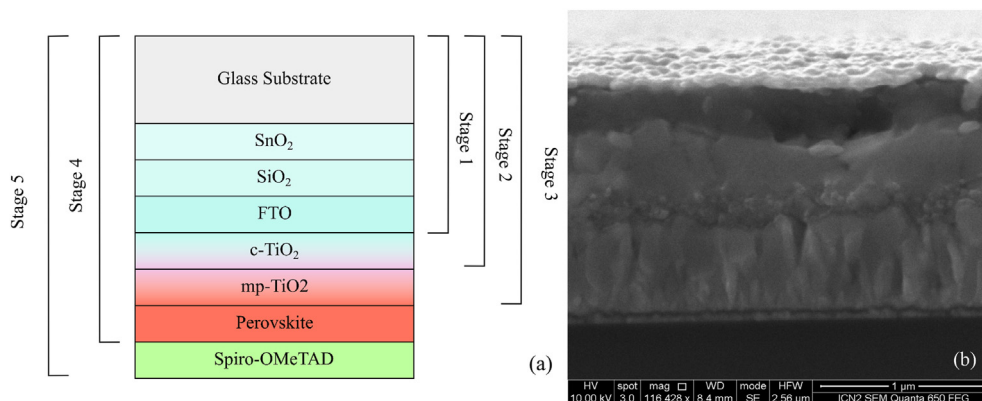

Fig. 1. (a) Structure of the layers present in each manufacturing stage. A total of five stages in which the optical behavior has been studied. (b) Typical cross-section image of the sample, obtained by means of the scanning electron microscope.

been measured for a similar perovskite. The physical characteristics of all layers that form the architecture of our device are displayed in Table 1.

On the other hand, if the layer contains a few constituents there is a need for some effective approach. The refractive index of the glass has been calculated from transmittance experimental measurements, while for the mp-TiO$_2$ material, we have developed an effective approach to determine its complex refractive index (see below).

2.3. Glass complex refractive index

Since the glass substrate consists of a few thin components, to determine the glass optical properties itself, the oxide films have to be removed. To this aim, on the glass multilayer system, the etching process is done by using Zn powder and HCl solution. As a result, the optical properties of the glass substrate have been determined with the aid of the method [45], based on the ideas discussed below.

If the slab of material has plane-parallel faces, and a material is absorbing partially ($k^2 \ll n$), the real part n and the imaginary part k of the refractive index of the slab can be calculated from the intensity of reflectance $R(\lambda) \equiv R$ and transmittance $T(\lambda) \equiv T$ spectra (for the sake of convenience we omit the symbol λ). In particular, the following analytical formulas have been used:

$$k = \frac{\lambda}{4\pi d} \ln\left[\frac{R_F \cdot T}{R - R_F}\right], \tag{1}$$

$$n = \frac{1 + R_F}{1 - R_F} + \left[\frac{4R_F}{(1 - R_F)^2} - k^2\right]^{1/2}, \tag{2}$$

where the slab geometrical thickness, d, is assumed as known, and

transport. However, in many simulations (see, for example, [46–49]) the effect of the porosity of the mesoporous TiO$_2$ layer on optical and electronic properties of meso-structured PSCs is ignored.

The presence of mesoporous thin films requires a proper approach to determine its optical characterization. Several effective medium approximations have been suggested to describe the optical properties of heterogeneous thin films by considering them as a homogeneous media with an effective refractive index, along with effective absorption coefficient. Most of the models have been developed for the effective refractive index omitting the absorption coefficient (see for a review [50]). However, the absorption can affect the optoelectronic properties of ETM, and, consequently, the properties of the whole system.

To consider the complex refractive index we apply the Volume Average Theory (VAT) model, discussed among others in Ref. [50]. It provides the effective complex refractive index (subindex eff) of a material (see Eqs. (4)–(7)) composed of a continuous phase material matrix (subindex c) and a dispersed phase material matrix (subindex d), with a porosity p:

$$n_{eff}^2 = \frac{1}{2}(A + \sqrt{A^2 + B^2}) \tag{4}$$

$$k_{eff}^2 = \frac{1}{2}(-A + \sqrt{A^2 + B^2}) \tag{5}$$

$$A = p(n_d^2 - k_d^2) + (1 - p)(n_c^2 - k_c^2) \tag{6}$$

$$B = 2pn_dk_d + 2(1 - p)n_ck_c \tag{7}$$

The properties of the mp-TiO$_2$ material can be characterized using an effective medium that contains a mixture of the c-TiO$_2$ material

$$R_F = (2 + T^2 - (1 - R)^2 - \{[2 + T^2 - (1 - R)^2]^2 - 4R(2 - R)\}^{1/2})(2(2 - R))^{-1}. \tag{3}$$

Experimental results for the transmittance $T(\lambda)$ and reflectance $R(\lambda)$ spectra, and the complex refractive index, obtained by means of Eqs. (1)–(3), are shown in Fig. 2.

2.4. Mesoporous layer as an effective medium: an optical approach

Mesoporous TiO$_2$ is one of the commonly used electron transport materials (ETMs) in PSCs. The mp-TiO$_2$ film serves not only as a scaffold for the perovskite layer but also as a route for electron

and air, as suggested in Refs. [51–53]. In the latter paper, however, the effect of the extinction coefficient k is missing. Evidently, it may play an important role, since the absorption in the mp-TiO$_2$ layer depends on the degree of its porosity.

To find thickness configurations that match best the experimental results, we developed a special procedure to quantify the minimal deviation of the theoretical estimations from the experimental values for the transmittance and the short-circuit current (see Figs. S4–S5 and the accompanying text). Once the above

Table 1

Characteristics of the considered semiconductors: TiO$_2$, FAPbI$_3$ (Perovskite), Spiro-OMeTAD. We use the following notations: χ is an electron affinity; E_g is an energy gap; $m_{e/h}^\star$ is an effective electron/hole mass; $N_{d/a}$, is a donor/acceptor concentration; μ is a mobility; ε is a permittivity; ℓ_D is a diffusion length.(**) The definition of the permittivity of the mp-TiO$_2$ is discussed in Sec.2.2; see Eq. (10) and the accompanying discussion.

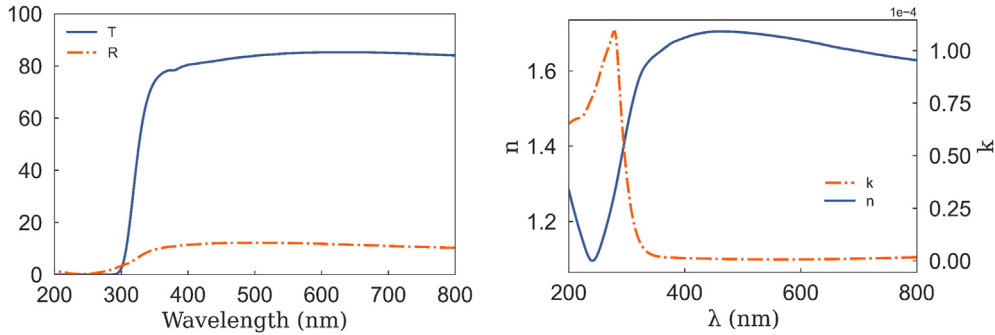| Input parameters in our calculations (References)				
	c-TiO$_2$	mp-TiO$_2$	Perovskite	Spiro-OMeTAD
χ [eV]	4 [35]	4 [35]	3.75 [36]	2.12 [37]
E_g [eV]	3.05 [38]	3.05 [38]	1.66 [34]	3.1 [39]
$m_e^\star$	1	1	1	1
$m_h^\star$	1	1	1	1
$N_{d/a}$[cm^{-3}]	1×10^{18}	variable	0	1×10^{21}
μ [cm^2/Vs]	0.006 [40]	0.006 [40]	variable	0.0001 [41]
ε	60 [42]	42.45**	60 [43]	3 [44]
ℓ_D[nm]	4	4	variable	0.5

Fig. 2. Left panel: the results of transmittance and reflectance measurements of the glass substrate as a function of the wavelength are shown. Right panel: the real (n) and imaginary (k) components of the calculated complex refractive index of the glass substrate as a function of the wavelength are displayed.

analysis has been completed, to gain much more accurate results on the optical properties of the PSC we use the OTSun python package.

2.5. Impact of porosity and Lambertian scattering

The knowledge of the thickness configuration enables to us to simulate the photogeneration rate for its application in the electronic transport equations. For the sake of convenience, we recapitulate briefly the basic steps of this procedure (see details in Ref. [23]).

According to the Beer-Lambert law for a given absorption coefficient $\alpha(\lambda) = 4\pi k(\lambda)/\lambda$ of a material, the loss of light intensity is a function of the path length ℓ of the light beam through a material:

$$N(\ell, \lambda) = N_0(0, \lambda)e^{-\alpha(\lambda)\ell}. \tag{8}$$

Here, $N_0(0, \lambda)$ is the initial number of photons of the incident ray on a material per unit area, per wavelength, and per unit time (for each time when a ray impacts onto a material according to the path trajectories determined by the ray tracing simulation). With the aid of OTSun and Eq. (8), we calculate the generation rate produced by a single ray

$$G(z) = \int_0^\infty \frac{\alpha(\lambda)N_0(0, \lambda)}{\cos\theta}e^{-\alpha(\lambda)z/\cos\theta}d\lambda, \tag{9}$$

where $z = \ell\cos\theta$ is the depth from a semiconductor surface, and θ is the ray-refracted angle. The function $G(z)$ provides the number of electrons per unit volume and per unit time, generated at each point in the device due to the photon absorption. The total function $G(z)$ is the sum of all rays (transmitted or reflected) passed at the point z. As a result, the obtained PSC thickness configuration and the rate function $G(z)$ allow to calculate the J-V characteristics by means of the transport model [23]. In this model, there is a set of parameters that are relatively well established either from literature or from measurements. Besides, there is another set that consists of some uncertain parameters. All of them are listed in Table 1, where uncertain parameters are named as "variable". The latter ones are treated as fitting parameters to explain the measured data.

There are a few comments in order, however. At this stage, we have to elaborate the model [23], taking into account the presence of the mp-TiO$_2$ layer. Consequently, to carry out the calculations within the transport model we have to define the permittivity and the conductivity of the mp-TiO$_2$ layer $\sigma_{mp} = q\mu_{mp}N_{mp}$; here μ_{mp} is a majority carrier mobility, and N_{mp} is the doping concentration.

From the optical properties of different layers, we obtain the fact that the mp-TiO$_2$ layer includes air-filled holes (porosity). As the

concentration of these holes is small ($\sim 20\%$), we apply the electrodynamic approach developed for weakly mixed systems (see the textbook [54]). In this case, the permittivity of the mp-TiO$_2$ material is provided by the expression for permittivity of the mixture ε_{mix}:

$$\varepsilon_{mix} = \varepsilon_{TiO_2} + \frac{3(\varepsilon_a - \varepsilon_{TiO_2})\varepsilon_{TiO_2}}{\varepsilon_a + 2\varepsilon_{TiO_2}}, \tag{10}$$

where ε_{TiO_2} and ε_a are the permittivities of TiO$_2$ and air, respectively. As for the conductivity, we make use of the fact obtained from the optical properties fitting. Due to a small concentration of air-filled holes in the mp-TiO$_2$ layer, one can suppose that the conductivity in this layer should be reduced to 20% as well. As a result, it seems reasonable to assume that the donor concentration holds the relation $N_{mp} = 0.8 \cdot N_c$, while the mobility of the carriers remains the same $\mu_{mp} = \mu_c$, as in the c-TiO$_2$ layer (see Sec.3) To obtain the better agreement with the J-V characteristics of our experimental device, we propose to vary only the unknown parameters N_{mp}, the mobility of carriers μ and their relaxation time τ in the perovskite layer, keeping the other parameters fixed.

It is important to stress that OTSun provides a more accurate form of the photogeneration rate $G(z)$ compared to the TMM approach used in the Supplementary Material, since non-specular reflection and multiple reflection are considered. In particular, from images obtained with the aid of the scanning electron microscope (see Fig. 1(b) and Fig. S3) it can be seen that the gold layer (the top layer) has nano-sized roughness, of the order of magnitude of its thickness (~ 80 nm). With a high degree of certainty, it can be argued that these textures provide a Lambertian reflection to the
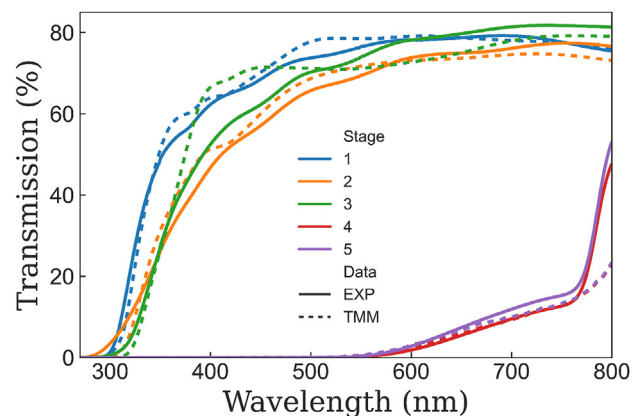

Fig. 3. Experimental (solid line) and theoretical (dotted line) transmittance curves for the different manufacturing stages of the PSCs under study. For the stage identifications see also Fig. 1
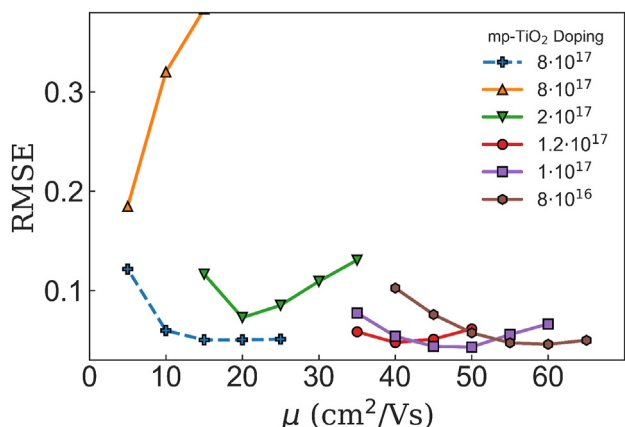
Fig. 4. RMSE as a function of carrier mobility in perovskite for different doping concentrations in the mp-TiO₂ layer. The solid curves are associated with the results of calculations without any additional resistances. The dotted line is associated with the results obtained by means of the additional resistances (see details in the text).

surface. Such textures randomly reflect the light that impacts on the gold layer, and, consequently, increase the optical path in the perovskite, and the photocurrent (cf. [11]). As a result, taking into account all the facts above, we obtain by means of (Eq. (9), Fig. S5) that $J_{sc} = 20.15$ mA/cm², i.e., it is slightly higher than the TMM result and closer to the experimental value.

3. Results and discussion

To begin with, we recall the main result of the analysis of the layer thicknesses (see details in Supplementary Material). The layer configuration chosen as the theoretical model of the PSCs studied is (in nm): 11 (SiO₂), 16 (SnO₂), 565 (FTO), 24 (c-TiO₂), 240 (mp-TiO₂, porosity = 20%), 500 (Perovskite), 250 (Spiro-OMeTAD). The result of this final disposition that produces the best consistency between theoretical and experimental values for the short-circuit current and the optical transmittance in each stage of the manufacturing process is displayed in Fig. 3.

There is a rather good agreement between experimental and theoretical results, except two cases: stages 3 and stage 4. The visible difference between the experimental and theoretical curves is located in the wavelength region 380 − 500 nm. This result implies some inaccuracy in estimation of the mp-TiO₂ layer absorption coefficient. Theoretical result exhibits the larger absorption for the perovskite FAPbI₃ (stage 4) in comparison with that of the

experimental sample in the wavelength range 770 − 800 nm. This disagreement is due to the difference between the experimental value of the perovskite absorption coefficient and that adopted from Ref. [34]. Since this difference is located at a small interval $760 < \lambda \leq 800$ nm of the right boundary of the considered wavelength region, it may be safely ignored in the description of the J-V characteristics discussed below.

The values of theoretical layer thicknesses and material parameters (see Table 1) are used as the input parameters in the electronic transport model to fit the simulated and measured J-V characteristics of the PSC. The fitting procedure is described in Ref. [23] but here we mention some peculiarities.

1. The main source of difference between the simulated and the measured short-circuit current has been related in Ref. [23] to the reflection properties of the PSC layers. In the present paper, the reflection properties are already taken into account by our optical model. It results in the remarkable accord between theoretical and experimental values of the short-circuit current (see below);

2. To fit the simulated and "measured averaged" open circuit voltage (V_{oc}) one needs to vary the carrier lifetimes (τ) in the perovskite [23]. Once we vary the donor concentration N_{mp} and the mobility μ, it is required to fit a τ-value to reproduce the experimental value of V_{oc}. To control the accuracy of the fitting procedure of J-V characteristics, we introduce the root mean square error.

$$RMSE = \frac{1}{N} \sqrt{\sum_i [J_{sc}^{exp}(V_i) - J_{sc}^{th}(V_i)]^2}, \qquad (11)$$

where the number of steps N is defined by the voltage range interval $V = 0 - V_{oc}$ passed with a step size ΔV. At each new value of the voltage $V_i = i \cdot \Delta V$, we solve the system of nonlinear transport equations (see Sec.2.4 in Ref. [23]) to calculate the current and compare its value with the experimental data. The results of calculations manifest the dependence of the RMSE on values of N_{mp} and the mobility μ (see Fig. 4).

We recall that the analysis of the transmittance resulted in a degree of porosity of the order of 20% for the mp-TiO₂ layer. Evidently, the presence of the porosity in the mp-TiO₂ layer should affect the donor concentration in this material in comparison to that in the c-TiO₂ layer, which is $1 \cdot 10^{18}$ cm⁻³ (see Table 1). Consequently, it is natural to suppose that the donor concentration
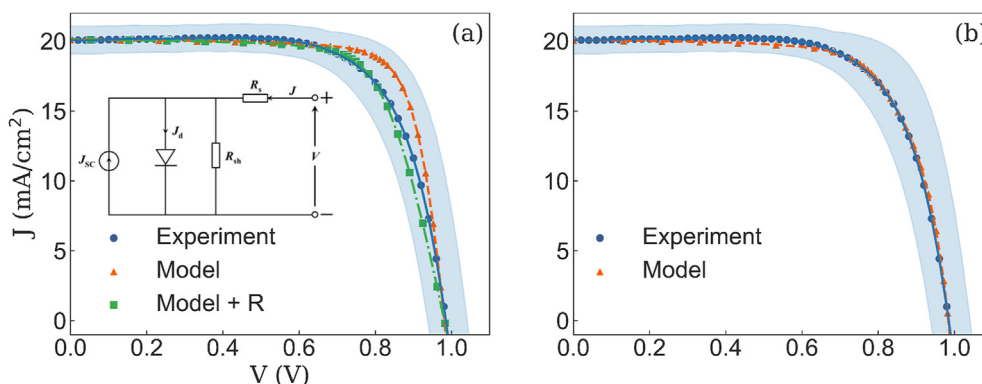

Fig. 5. J-V characteristics. In panels (a) and (b) solid line connecting solid circles is associated with the "measured averaged" values. The panel (a): dashed (dot-dashed) line connecting solid triangles (squares) is associated with the results obtained without (with) additional resistances at 20% porosity of mp-TiO₂ layer. The panel (b): dashed line connecting solid triangles is associated with the results obtained without additional resistances (see for details the text). Light blue band around all these curves marks the range in which the measured J-V characteristics of different samples lie. The insert in the panel (a) displays the circuit layout of the generator.

Table 2

Main PSC parameters for the "measured averaged" device and simulated results obtained by means of our approach. Model (a) is associated with results displayed on the panel Fig. 5(a), without any resistance; the corresponding parameters are presented in the first column of Table 3. Model (a) + R is associated with results displayed on the panel Fig. 5(a), with resistance; the corresponding parameters are presented in the second column of Table 3. Model (b) is associated with results displayed on the panel Fig. 5(b); the corresponding parameters are presented in the third column of Table 3.

	J_{sc} (mA/cm^2)	V_{oc} (V)	FF	PCE(%)
Experiment	20.072	0.985	0.695	13.735
Model (a)	20.120	0.981	0.772	15.233
Model (a) + R	20.101	0.981	0.705	13.903
Model (b)	20.076	0.984	0.703	13.882

in the mp-TiO$_2$ layer will decrease to the value $8 \cdot 10^{17}$ cm^{-3}, proportionally to the degree of its porosity. Taking into account that the porosity affects the permittivity (see Eq. (10)) and the donor concentration of the mp-TiO$_2$ layer, we solve the transport equations and reach the RMSE minimum (0.18 mA/cm^2) at $\mu = 5$ cm^2/(V·s) (see Fig. 4; triangles connected by solid yellow line). There is a visible difference between the simulated and the "measured averaged" J-V characteristics (see Fig. 5(a)).

A fairly common trick in the calculation of J-V characteristics is to use the analogy of the PSC to a current generator in parallel with a diode (see, for example, the analysis in Ref. [11]). Hereafter we follow this procedure since such an approach enables us to consider the parasitic resistance of the contacts and feeding conductors, R; the leakage resistance, related to the local short-circuit of electron/hole transport material layers, R$_{sh}$ (see the insert in Fig. 5(a)).

Once all necessary additional resistances are generated, we obtain a good agreement of our results with the experimental J-V characteristics. This agreement (see Fig. 5(a)) is reached with the aid of the following values of the variable parameters: $\mu = 15$ cm^2/(V·s) (see Fig. 4); R = 4 Ohm·cm^2; R$_{sh} \to \infty$; $\tau = 2.47$ ns that yields the diffusion length $\ell_D = \sqrt{\mu k_B T \tau / |e|} = 0.3$ μm.

It turns out, however, that we can obtain even better agreement by varying the donor concentration in the mp-TiO$_2$ layer. The variation of the RMSE between simulated and "measured averaged" J-V characteristics yields the RMSE absolute minimum (see Fig. 4) at the "optimal" mobility $\mu = 50$ cm^2/(V·s), and the donor concentration $N_{mp} = 1 \cdot 10^{17}$ cm^{-3}. The optimal carrier lifetimes $\tau = 0.7$ ns yields again the diffusion length $\ell_D = 0.3$ μm. At these parameters, we obtain a remarkable agreement between the simulated and the "measured averaged" J-V characteristics, without any additional resistances (see Fig. 5(b)). It seems that in the mp-TiO$_2$ layer pore holes generate all necessary additional resistance in the measured device.

Consequently, it appears that in the real device, the pore dimension occupying 20% of the mp-TiO$_2$ layer is sufficient to affect optical properties of the PSC. It turns out, however, that only a small part of the remaining TiO$_2$ take part in the conductance due to a large amount of defects on the pore boundaries.

It is noteworthy that the parameters values obtained by means of our fitting procedure are located within the parameter range considered in literature. In particular, several studies suggest that the doping values of the mp-TiO$_2$ material are in the range of 10^{16} to

Table 3

Summary of the parameters used to represent Fig. 5 and Table 2.

Parameters	Model (a)	Model (a) + R	Model (b)
N_{mp} (cm^{-3})	$8 \cdot 10^{17}$	$8 \cdot 10^{17}$	$1 \cdot 10^{17}$
μ (cm^2/(V·s))	15	15	50
τ (ns)	2.47	2.47	0.7
R (Ohm·cm^2)	–	4	–
R$_{sh}$ (Ohm·cm^2)	–	∞	–

10^{19} (cm^{-3}) [55]. Moreover, the carrier mobility range measured for perovskite is in the range from 5 to 50 (cm^2/(V·s)) [56]. The degree of the accuracy of our analysis is summarized in Tables 2 and 3. It demonstrates that the short-circuit current, the open circuit voltage, the fill factor, and the PCE for both simulated and experimental PSC are in remarkable agreement.

4. Conclusions

In summary, we have successfully utilized the optoelectronic model based on experimentally obtained optical features for planar meso-structured PSCs. Our optoelectronic model incorporates ray tracing simulations, the transfer-matrix method, and the carrier transport equations. The ray tracing allows the exploration of any geometry, since the solar collector device is designed by means of the FreeCAD software. The combination of ray tracing with the transfer-matrix method allows to perform the optical simulations considering Fresnel optics, internal reflections of the multilayer system, scattering produced by nanoroughness layers, and effective layers with some peculiarities (such as porous materials).

Large number of transmittance-reflectance measurements on the several stages of manufacturing process have been used to fix the uncertainties of the PSC layer's thicknesses and the mesoporous TiO$_2$ layer porosity. The same number of measurements have been done to define the average J-V characteristics of experimental devices. The obtained results within the optoelectronic model have been further used to analyze J-V characteristics of the manufactured PSCs by means of the optimization procedure based on the multiple-use of the solution transport equations [23]. The developed model demonstrates good agreement with both optical and electrical measurements leading to extraction of the layers' thicknesses, the porosity degree and the permittivity of the mesoporous TiO$_2$ material, the perovskite carrier's mobility and lifetimes. In addition, we have found that even a small degree of the porosity can affect the performance of the experimental devices, reducing essentially the effective donor concentration (i.e., the conductance) of the mp-TiO$_2$ layer in comparison to that in the c-TiO$_2$ layer.

Our approach allows the study of devices with different architectures. Reversing the order of the materials in the solar cell structure does not affect the development of the optoelectronic simulations. Thus, our work provides a useful platform for device optimization towards increasing PCE as well as appropriate tools for the analysis of various optoelectronic properties of meso-structured PSCs.

Author contributions

The plan was conceived and planned by F. Bonnín-Ripoll and R. Pujol-Nadal, coordinated also with M. Lira-Cantú. The manufacture of the samples was performed by K. Tabah, C. Pereyra, supervised by M. Lira-Cantú. The spectrophotometry and optical analysis were in charge of F. Bonnín-Ripoll, as well as the optical calculations, supervised by R. Pujol-Nadal. Ya. B. Martynov wrote the code and, together with F. Bonnín-Ripoll, perform the electronic transport calculations. G. Cardona and R. Pujol-Nadal wrote the OTSun code and the latter perform the simulations on this software. F. Bonnín-Ripoll prepared the initial draft of the manuscript. R. G. Nazmitdinov coordinated the analysis of results and wrote the final version of the manuscript.

Declaration of competing interest

The authors declare that they have no known competing financial interests or personal relationships that could have appeared to influence the work reported in this paper.

Data availability

Data will be made available on request.

Acknowledgments

Appendix A. Supplementary data

Supplementary data to this article can be found online at https://doi.org/10.1016/j.mtsust.2023.100548.

References

[1] H. Min, D.Y. Lee, J. Kim, G. Kim, K.S. Lee, J. Kim, M.J. Paik, Y.K. Kim, K.S. Kim, M.G. Kim, T.J. Shin, S. Il Seok, Perovskite solar cells with atomically coherent interlayers on SnO2 electrodes, Nature 598 (2021) 7881, https://doi.org/10.1038/s41586-021-03964-8, 598 (7881) (2021) 444−450.
[2] V. Babu, R. Fuentes Pineda, T. Ahmad, A.O. Alvarez, L.A. Castriotta, A. Di Carlo, F. Fabregat-Santiago, K. Wojciechowski, Improved stability of inverted and flexible perovskite solar cells with carbon electrode, ACS Appl. Energy Mater. 3 (6) (2020) 5126−5134, https://doi.org/10.1021/acsaem.0c00702.
[3] Y.B. Martynov, R.G. Nazmitdinov, A. Moià-Pol, P.P. Gladyshev, A.R. Tameev, A.V. Vannikov, M. Pudlak, On the efficiency limit of ZnO/CH3NH3PbI3/CuI perovskite solar cells, Phys. Chem. Chem. Phys. 19 (2017) 19916−19921, https://doi.org/10.1039/C7CP03892E.
[4] R. Urzúa-Leiva, A. Narymany Shandy, H. Xie, M. Lira-Cantú, G. Cárdenas-Jirón, Effects of the methylammonium ion substitution by 5-ammoniumvaleric acid in lead trihalide perovskite solar cells: a combined experimental and theoretical investigation, New J. Chem. 44 (34) (2020) 14642−14649, https://doi.org/10.1039/D0NJ02748K.
[5] A. Frontera, Y. Martynov, R.G. Nazmitdinov, A. Moià-Pol, Perovskite: material and device optimization for solar cell applications, in: Perovskite Solar Cells: Properties, Application and Efficiency, Nova Science Publishers/Inc., 2019, pp. 117−174. Ch. 3.
[6] A. Agresti, A. Pazniak, S. Pescetelli, A. Di Vito, D. Rossi, A. Pecchia, M. Auf der Maur, A. Liedl, R. Larciprete, D.V. Kuznetsov, D. Saranin, A. Di Carlo, Titanium-carbide MXenes for work function and interface engineering in perovskite solar cells, Nat. Mater. 18 (2019) 1228−1234, https://doi.org/10.1038/s41563-019-0478-1.
[7] Y.B. Martynov, R.G. Nazmitdinov, P.P. Gladyshev, A. Moià-Pol, Effect of contact barrier heights on the power conversion efficiency of a perovskite photovoltaic element, Mendeleev Commun. 31 (4) (2021) 459−461, https://doi.org/10.1016/j.mencom.2021.07.007.
[8] T. Li, S. Wang, J. Yang, X. Pu, B. Gao, Z. He, Q. Cao, J. Han, X. Li, Multiple functional groups synergistically improve the performance of inverted planar perovskite solar cells, Nano Energy 82 (2021), https://doi.org/10.1016/J.NANOEN.2021.105742.
[9] X. Zhang, J. Wu, S. Wang, W. Pan, M. Zhang, X. Wang, Z. Lan, J. Lin, Additive engineering by 6-aminoquinoline monohydrochloride for high-performance perovskite solar cells, ACS Appl. Energy Mater. 4 (2021), https://doi.org/10.1021/ACSAEM.1C01142.
[10] C. Pereyra, H. Xie, M. Lira-Cantu, Additive engineering for stable halide perovskite solar cells, J. Energy Chem. 60 (2021) 599−634, https://doi.org/10.1016/J.JECHEM.2021.01.037.
[11] F. Bonnín-Ripoll, Y.B. Martynov, G. Cardona, R.G. Nazmitdinov, R. Pujol-Nadal, Synergy of the ray tracing+carrier transport approach: on efficiency of perovskite solar cells with a back reflector, Sol. Energy Mater. Sol. Cell. 200 (2019) 110050, https://doi.org/10.1016/j.solmat.2019.110050.
[12] K. Deng, L. Li, K. Deng, L. Li, Optical design in perovskite solar cells, Small Methods (2019), https://doi.org/10.1002/smtd.201900150.
[13] G. Haidari, Comparative 1D optoelectrical simulation of the perovskite solar cell, AIP Adv. (2019), https://doi.org/10.1063/1.5110495.
[14] A.K. Mishra, R.K. Shukla, Electrical and optical simulation of typical perovskite solar cell by GPVDM software, Mater. Today: Proc. 49 (2020) 3181−3186, https://doi.org/10.1016/J.MATPR.2020.11.376.
[15] A. Husainat, W. Ali, P. Cofie, J. Attia, J. Fuller, A. Darwish, Simulation and analysis method of different back metals contact of CH3NH3PbI3 perovskite solar cell along with electron transport layer TiO2 using MBMT-MAPLE/PLD, Am. J. Opt. Photon. 8 (1) (2020) 6, https://doi.org/10.11648/J.AJOP.20200801.12.
[16] M. Al-Hattab, L. Moudou, M. Khenfouch, O. Bajjou, Y. Chrafih, K. Rahmani, Numerical simulation of a new heterostructure CIGS/GaSe solar cell system using SCAPS-1D software, Sol. Energy 227 (2021), https://doi.org/10.1016/J.SOLENER.2021.08.084.
[17] S.S. Hussain, S. Riaz, G.A. Nowsherwan, K. Jahangir, A. Raza, M.J. Iqbal, I. Sadiq, S.M. Hussain, S. Naseem, Numerical modeling and optimization of lead-free hybrid double perovskite solar cell by using SCAPS-1D, Journal of Renewable Energy 2021 (2021), https://doi.org/10.1155/2021/6668687.
[18] R.K. Yadav, P.S. Pawar, R. Nandi, K.R.E. Neerugatti, Y.T. Kim, J.Y. Cho, J. Heo, A qualitative study of SnSe thin film solar cells using SCAPS 1D and comparison with experimental results: a pathway towards 22.69% efficiency, Sol. Energy Mater. Sol. Cell. (2022) 244, https://doi.org/10.1016/J.SOLMAT.2022.111835.
[19] K. Ahmad, M.Q. Khan, R.A. Khan, H. Kim, Numerical simulation and fabrication of Pb-free perovskite solar cells (FTO/TiO2/Cs3Bi2I9/Spiro-OMeTAD/Au), Opt. Mater. 128 (2022), https://doi.org/10.1016/J.OPTMAT.2022.112458.
[20] S. Karthick, S. Velumani, J. Bouclé, Chalcogenide BaZrS3 perovskite solar cells: a numerical simulation and analysis using SCAPS-1D, Opt. Mater. 126 (2022), https://doi.org/10.1016/J.OPTMAT.2022.112250.
[21] M. Burgelman, K. Decock, A. Niemegeers, J. Verschraegen, S. Degrave, SCAPS-1D Manual, 2021.
[22] K. Deepthi Jayan, V. Sebastian, Comprehensive device modelling and performance analysis of MASnI3 based perovskite solar cells with diverse ETM, HTM and back metal contacts, Sol. Energy 217 (2021) 40−48, https://doi.org/10.1016/J.SOLENER.2021.01.058.
[23] F. Bonnín-Ripoll, Y.B. Martynov, R.G. Nazmitdinov, G. Cardona, R. Pujol-Nadal, On the efficiency of perovskite solar cells with a back reflector: effect of a hole transport material, Phys. Chem. Chem. Phys. (2021), https://doi.org/10.1039/D1CP03313A.
[24] H. Xie, Z. Wang, Z. Chen, C. Pereyra, M. Pols, K. Gałkowski, M. Anaya, S. Fu, X. Jia, P. Tang, D.J. Kubicki, A. Agarwalla, H.S. Kim, D. Prochowicz, X. Borrisé, M. Bonn, C. Bao, X. Sun, S.M. Zakeeruddin, L. Emsley, J. Arbiol, F. Gao, F. Fu, H.I. Wang, K.J. Tielrooij, S.D. Stranks, S. Tao, M. Grätzel, A. Hagfeldt, M. Lira-Cantu, Decoupling the effects of defects on efficiency and stability through phosphonates in stable halide perovskite solar cells, Joule 5 (5) (2021) 1246−1266, https://doi.org/10.1016/J.JOULE.2021.04.003.
[25] H. Liu, Z. Huang, S. Wei, L. Zheng, L. Xiao, Q. Gong, Nano-structured electron transporting materials for perovskite solar cells, Nanoscale 8 (12) (2016) 6209−6221, https://doi.org/10.1039/c5nr05207f.
[26] G. Cardona, R. Pujol-Nadal, OTSun, a python package for the optical analysis of solar-thermal collectors and photovoltaic cells with arbitrary geometry, PLoS One 15 (10) (2020) e0240735, https://doi.org/10.1371/journal.pone.0240735.
[27] R. Pujol-Nadal, G. Cardona, OTSunWebApp: A ray tracing web application for the analysis of concentrating solar-thermal and photovoltaic solar cells, Software X 23 (2023) 101449, https://doi.org/10.1016/j.softx.2023.101449.
[28] S. Byrnes, tmm 0.1.7 : Python Package Index, 2017. URL, https://pypi.python.org/pypi/tmm.
[29] S.J. Byrnes, Multilayer Optical Calculations, 2020 arXiv:1603.02720.
[30] FreeCAD, Your own 3D parametric modeler. https://www.freecadweb.org/, 2001.
[31] E. Ching-Prado, A. Watson, H. Miranda, Optical and electrical properties of fluorine doped tin oxide thin film, J. Mater. Sci. Electron. 29 (18) (2018) 15299−15306, https://doi.org/10.1007/s10854-018-8795-8.
[32] T. Siefke, S. Kroker, K. Pfeiffer, O. Puffky, K. Dietrich, D. Franta, I. Ohlídal, A. Szeghalmi, E.-B. Kley, A. Tünnermann, Materials pushing the application limits of wire grid polarizers further into the deep ultraviolet spectral range, Adv. Opt. Mater. 4 (11) (2016) 1780−1786, https://doi.org/10.1002/adom.201600250.
[33] C.W. Chen, S.Y. Hsiao, C.Y. Chen, H.W. Kang, Z.Y. Huang, H.W. Lin, Optical properties of organometal halide perovskite thin films and general device structure design rules for perovskite single and tandem solar cells, J. Mater. Chem. A 3 (17) (2015) 9152−9159, https://doi.org/10.1039/C4TA05237D.
[34] H.W. Chen, D.P. Gulo, Y.C. Chao, H.L. Liu, Characterizing temperature-dependent optical properties of (MA0.13FA0.87) PbI3 single crystals using

spectroscopic ellipsometry, Sci. Rep. (1) (2019) 1−9, https://doi.org/10.1038/s41598-019-54636-7, 2019 9:1 9.

[35] F. Liu, J. Zhu, J. Wei, Y. Li, M. Lv, S. Yang, B. Zhang, J. Yao, S. Dai, Numerical simulation: toward the design of high-efficiency planar perovskite solar cells, Appl. Phys. Lett. 104 (2014) 253508, https://doi.org/10.1063/1.4885367.

[36] A. Hima, Simulation and optimization of CH3NH3PbI3 based inverted planar heterojunction solar cell using SCAPS software, Int. J. Energetica 4 (2019) 56−59, https://doi.org/10.47238/ijeca.v4i1.92.

[37] F. Zhang, Z. Wang, H. Zhu, N. Pellet, J. Luo, C. Yi, X. Liu, H. Liu, S. Wang, X. Li, Y. Xiao, S.M. Zakeeruddin, D. Bi, M. Grätzel, Over 20% PCE perovskite solar cells with superior stability achieved by novel and low-cost hole-transporting materials, Nano Energy 41 (2017) 469−475, https://doi.org/10.1016/j.nanoen.2017.09.035.

[38] A. Farhana, R. Mahbub, S.S. Satter, S.M. Ullah, Effect of different HTM layers and electrical parameters on ZnO nanorod-based lead-free perovskite solar cell for high-efficiency performance, Int. J. Photoenergy 9 (2017) 9846310, https://doi.org/10.1155/2017/9846310, 2017.

[39] X. Wang, L.-L. Deng, L.-Y. Wang, S.-M. Dai, Z. Xing, X.-X. Zhan, X.-Z. Lu, S.-Y. Xie, R.-B. Huang, L.-S. Zheng, Cerium oxide standing out as an electron transport layer for efficient and stable perovskite solar cells processed at low temperature, J. Mater. Chem. A 5 (2017) 1706−1712, https://doi.org/10.1039/C6TA07541J.

[40] K. Wojciechowski, M. Saliba, T. Leijtens, A. Abate, H.J. Snaith, Sub-150°C processed meso-superstructured perovskite solar cells with enhanced efficiency, Energy Environ. Sci. 7 (2014) 1142−1147, https://doi.org/10.1039/C3EE43707H.

[41] H.J. Snaith, M. Grätzel, Enhanced charge mobility in a molecular hole transporter via addition of redox inactive ionic dopant: implication to dye-sensitized solar cells, Appl. Phys. Lett. 89 (2006) 262114, https://doi.org/10.1063/1.2424552.

[42] S. Dutta, Leeladhar, A. Pandey, O.P. Thakur, R. Pal, Electrical properties of ultrathin titanium dioxide films on silicon, J. Vac. Sci. Technol. A 33 (2015) 021507, https://doi.org/10.1116/1.4904978.

[43] M. Green, A. Ho-Baillie, H. Snaith, The emergence of perovskite solar cells, Nat. Photonics 8 (2014) 506−514, https://doi.org/10.1038/nphoton.2014.134.

[44] J. García-Cañadas, F. Fabregat-Santiago, H.J. Bolink, E. Palomares, G. Garcia-Belmonte, J. Bisquert, Determination of electron and hole energy levels in mesoporous nanocrystalline TiO2 solid-state dye solar cell, Synth. Met. 156 (2006) 944−948, https://doi.org/10.1016/j.synthmet.2006.06.006.

[45] E. Nichelatti, Complex refractive index of a slab from reflectance and transmittance: analytical solution, J. Opt. Pure Appl. Opt. 4 (2002) 400−403, https://doi.org/10.1088/1464-4258/4/4/306.

[46] K.P. Kim, W.H. Kim, S.M. Kwon, J.Y. Kim, Y.S. Do, S. Woo, Enhanced light absorption by facile patterning of nano-grating on mesoporous TiO_2 photoelectrode for cesium lead halide perovskite solar cells, Nanomaterials 11 (2021) 1233 11, https://doi.org/10.3390/NANO11051233, 2021.

[47] E. Widianto, Shobih, E.S. Rosa, K. Triyana, N.M. Nursam, I. Santoso, Performance analysis of carbon-based perovskite solar cells by graphene oxide as hole transport layer: experimental and numerical simulation, Opt. Mater. 121 (2021), https://doi.org/10.1016/J.OPTMAT.2021.111584.

[48] M. Mehrabian, O. Akhavan, N. Rabiee, E.N. Afshar, E.N. Zare, Lead-free $MAGeI_3$ as a suitable alternative for $MAPbI_3$ in nanostructured perovskite solar cells: a simulation study, Environ. Sci. Pollut. Control Ser. 30 (2023), https://doi.org/10.1007/S11356-023-26497-1/FIGURES/6.

[49] M.K. Hossain, G.F. Toki, A. Kuddus, M.H. Rubel, M.M. Hossain, H. Bencherif, M.F. Rahman, M.R. Islam, M. Mushtaq, An extensive study on multiple ETL and HTL layers to design and simulation of high-performance lead-free $CsSnCl_3$-based perovskite solar cells, Sci. Rep. 13 (2023) 1 13, https://doi.org/10.1038/s41598-023-28506-2, 2023.

[50] N.J. Hutchinson, T. Coquil, A. Navid, L. Pilon, Effective optical properties of highly ordered mesoporous thin films, Thin Solid Films 518 (8) (2010) 2141−2146, https://doi.org/10.1016/J.TSF.2009.08.048.

[51] E. Raoult, R. Bodeux, S. Jutteau, S. Rives, A. Yaiche, D. Coutancier, J. Rousset, S. Collin, Optical characterizations and modelling of semitransparent perovskite solar cells for tandem applications, EU PVSEC Proceedings 36th (2019) 757−763, https://doi.org/10.4229/EUPVSEC20192019-3BV.2.53. EU PVSEC 2019.

[52] E. Raoult, R. Bodeux, S. Jutteau, S. Rives, A. Yaiche, A. Blaizot, D. Coutancier, J. Rousset, S. Collin, Iterative method for optical modelling of perovskite-based tandem solar cells, Opt Express 30 (6) (2022) 9604, https://doi.org/10.1364/OE.444698.

[53] A. Hernández-Granados, A.N. Corpus-Mendoza, P.M. Moreno-Romero, C.A. Rodríguez-Castañeda, J.E. Pascoe-Sussoni, O.A. Castelo-González, E.C. Menchaca-Campos, J. Escorcia-García, H. Hu, Optically uniform thin films of mesoporous TiO2 for perovskite solar cell applications, Opt. Mater. 88 (2019) 695−703, https://doi.org/10.1016/j.optmat.2018.12.044.

[54] L. Landau, E. Lifshitz, L. Pitaevskii, Electrodynamics of Continuous Media: Volume 8, Course of Theoretical Physics, Elsevier Science, 1995.

[55] M.C. Sellers, E.G. Seebauer, Measurement method for carrier concentration in TiO_2 via the Mott−Schottky approach, Thin Solid Films 519 (7) (2011) 2103−2110, https://doi.org/10.1016/J.TSF.2010.10.071.

[56] L.M. Herz, Charge-carrier mobilities in metal halide perovskites: fundamental mechanisms and limits, ACS Energy Lett. 2 (7) (2017) 1539−1548, https://doi.org/10.1021/acsenergylett.7b00276.